https://dx.doi.org/10.1016/j.conbuildmat.2017.08.098

Numerical Analysis and Punching Shear Fracture Based Design of Longitudinal Plate to Concrete-filled CHS Connections

Fei Xu[1,2], Ju Chen[1]* and Tak-Ming Chan[2]

1. Institute of Structural Engineering, Zhejiang University, Hangzhou, Zhejiang, 310058, PR China

2. Department of Civil and Environmental Engineering, The Hong Kong Polytechnic University, Hong Kong, 999077, PR China

Abstract: The mechanical behaviour of longitudinal plate-to-concrete-filled circular hollow section (CHS) connections under axial tension, eccentric tension and in-plane bending is extensively studied by the experimentally validated finite element analysis (FEA) in this paper. A total of 336 connections with a wide range of parameters on geometrical configurations, material properties and load positions was conducted to investigate a) the general applicability of the experimental conclusion for the governing limit state, b) the shear stress profiles on the failure face and c) the design equations based on fracture analytical models under various loading conditions. FEA extended the validity of experimental conclusion that the only governing limit state was ultimate strength at punching shear failure instead of the strength at deformation limit of 3% chord diameter (*D*). With an aim of proposing design equations based on fracture mechanics, the shear stress distributions on the failure face and the inner concrete was investigated by numerical parametric study, and then were adopted in the analytical models. Finally, design equations based on semi-theoretical models for the ultimate strength of longitudinal plate-to-concrete-filled CHS connections under three investigated loads were proposed. It is found the connection-capacity predictions agreed with both test and FEA results well.

Keywords: Concrete-filled steel tubes; Design; Finite element analysis; Longitudinal plate connections; Punching shear fracture

[1]Postdoctoral fellow, Department of Civil and Environmental Engineering, Hong Kong Polytechnic University, Hong Kong, PR China

[2]Associate Professor, Department of Civil Engineering, Zhejiang University, Hangzhou, P.R. China. (Corresponding author.) E-mail: cecj@zju.edu.cn

[3]Assistant Professor, Department of Civil and Environmental Engineering, The Hong Kong Polytechnic University, Hong Kong, PR China

© 2017. This manuscript version is made available under the CC-BY-NC-ND 4.0 license http://creativecommons.org/licenses/by-nc-nd/4.0/

1. Introduction

Concrete-filled steel circular hollow section (CHS) member is a popular alternative to hollow structural section (HSS) one especially when subjected to compression. It is due to the efficient utilization of the material strengths for both concrete and steel, leading to a better local bulking resistance and a higher ultimate strength, especially for those thin-walled members [1,2,3]. A simple and efficient way to connect those circular hollow section (CHS) members with branch members is to use a gusset plate, including longitudinal and transvers ones which are directly welded on the tube wall surface. Fig. 1 gives an example of a gusset plate-to-tube connection used in a large-span transmission tower in China. The longitudinal plate connection original from branch plate-to-I-beam connection is a traditional and common connection type especially for those with lightly loaded branch members. Because of the flexibility of the thin tube wall face which often causes the excessive deformation combined with chord ovalization, the capacity of those branch plate-to-CHS connections are thus often governed by the deformation limit state. Therefore special precautions, such as connection stiffening, are always taken into consideration in practical design.

Previous studies have proposed relevant methods to stiffen those tubular connections with a flexible face, such as a through plate connection [4,5,6], an annular ring stiffened connection [7,8,9], a concrete-filled connection [6,10]. It is found that for the first two mentioned stiffened connections (for hollow tubes), the tube wall deformation was decreased and the flexibility of connection face was mitigated, but the capacity was still governed by the deformation limit failed at the state of chord-wall plasitification; while for the concrete-filled connections, Voth [6] and Xu, *et al*. [10] showed that punching shear failure of chord-wall was the dominant limit state. They also indicate that the branch plate-to-CHS connections utilized the full strength of steel material. However the design recommendations for punching shear strength in CIDECT-1 [11] for non-concrete-filled plate connection, is generally conservative when applied to the inner concrete stiffened ones especially in the case of in-plane bending [10].

Significant research has been conducted on branch plate-to-HSS connection behaviour and design methods [5,12-18], some of which have been adopted in current design guidelines, such as CIDECT-1 [11] and CIDECT-3 [19] and codes of practice, API [20] and AISC 360-10 [21]. Unfortunately, limited experimental and numerical research [6,10] are available for the behaviour of plate-to-concrete-filled CHS connections, therefore there is a need to conduct complementary numerical simulation to propose design equations base on both experimental and numerical data. Thus, the method of finite element analysis (FEA) is employed to extend the scope of test specimens for both geometrical configurations and material properties. By a combined way of experimental and numerical investigations, the design recommendations for branch plate-to-concrete-filled CHS connections can be proposed with both a wider validity range and considerable reliability.

In this study, the mechanical behaviour of longitudinal plate-to-concrete-filled CHS connections under axial tension, eccentric tension and in-plane bending were extensively studied to further confirm the experimental observations upon the governing limit state and failure modes from FEA firstly. Secondly, the shear stress profiles on the failure face were also analysed and the distribution equations were proposed accordingly based on punching shear fracture. Thirdly, based on the determined governing limit state and failure modes, the analytical models for connections under each loading condition were established. Finally, design equations corresponding to the punching shear failure mode for axial/eccentric tension and in-plane bending loaded plate-to-concrete-filled CHS connection were proposed.

2. Summary of experimental investigation

2.1. Test program

Xu *et al*. [10] carried out tests of eleven longitudinal plate-to-concrete-filled-CHS connections under axial tension, eccentric tension and in-plane bending. The test set-up and specimens are shown in Fig. 2 with the measured geometrical dimensions of specimens presented in Table 1. The results of tensile coupon tests on the tube and plate materials are listed in Table 2. The cubic compressive strength (f_{cu}) and elastic modulus (E_c) of the in-fill concrete at 28 days were 46.9 MPa and 37420 MPa, respectively. Fillet welds were used to connect the longitudinal plate with CHS face. Fig. 2 also shows typical test set-ups and displacement measurement arrangements for specimens under each specified loading conditions. All test specimens were loaded by a 1000-kN-tension-capacity MTS actuator controlled by displacement at a speed of 0.5 mm/min. More detailed information of the test program is given in Xu *et al*. [10].

The test specimens are labeled as follows: the connection type, the chord diameter, the chord thickness and the loading condition in the test. For example, the label "T-300-4-E125" defines a T-connection with a nominal outer chord diameter of 300 mm and nominal chord thickness of 4 mm under eccentric tensile loading with eccentricity of 125 mm.

2.2. Test results

The test results reported by Xu *et al*. [10] showed that all test specimens failed in tube wall punching shear which was initiated from the chord tube face at the end of the plate, except for the one with 6-mm tube wall thickness under axial tension which was failed by brace yielding. Typical failure modes of specimens under different loading conditions are shown in Fig. 3. Moreover the measured average deformation at A and B points (for specimens under tension) and maximum deformation at B point (for specimens under eccentric tension and in-plane bending) at the ultimate strength (peak load) are lower than 3% chord diameter (D) as shown in Fig. 4. In Fig. 4 the measured experimental deformations at A and B were calculated as (δ_A-δ_{A1}) and (δ_B-δ_{B1}) which were attained from the recordings of LVDTs located at points A, A_1, B and B_1, 15 mm away from the weld toe, as shown in Fig. 2. For in-plane bending specimens, the moment was evaluated as the applied tensile load × force arm (790 mm in this study). This indicated that the connection capacity was governed by the maximum strength limit instead of the deformation limit. It was significantly different from the specifications in current design guidelines CIDECT-1 [11] which is applicable for plate-to-plain-CHS connections. The experimental connection strengths (F_{EXP}, M_{EXP} = F_{EXP} × 790 mm) and design strengths are compared in Table 1 and Fig. 5, respectively.

3. Finite element modeling and validation

3.1. Finite element (FE) modelling methodology and analysis

The FE models were established for replicating the experimental connections and subsequently extending experimental data to a large number of models with different parameters to investigate the general behaviour of longitudinal plate-to-concrete-filled connections. The FE models of plate-to-concrete-filled CHS connections were conducted using ABAQUS/Explicit [22]. For those FE models replicating the experimental connection, the geometrical dimensions followed the measured dimensions. In addition, the models in parametric study were built with a constant chord length of 1400 mm, a constant plate height (h_b) of 190 mm while the fillet welds were set to be capable of the full plate capacity, and the same loading area and concrete property as the test specimens under corresponding loading conditions. All other geometrical configurations and material properties varied in the parametric study, and therefore the varied parameters expressed in the specimen labels, for example the model T-300-4-E50 with plate length (l_b) of 500 mm and plate thickness (t_b) of 12 mm will be expressed as T-300-4-500-12-E50. Both ends of chord member were fixed with all degrees of freedom to be zero according to the end conditions in the test. For simplification, the brace member connected to the plate were omitted and a loading area line of connecting bolts was created in the case of axial and eccentric tension, whilst two rigid plates with the same force arm length as the brace were tied to the longitudinal plate connections under in-plane bending. The loads for each loading condition were applied accordingly at the same loading speed as in the test. More details for FE models are shown in Fig. 6.

All models were constructed by solid elements (C3D8R) with an element size near the connecting area (regions of high stress gradient) around 5 mm, an element size of 25 mm towards the ends of the chord and plate (regions of relative uniform stress) and a constant element size of

15 mm for infill concrete part. For the connecting area, the element size of 3 mm, 5 mm and 8 mm were used in the mesh sensitivity study as shown in Fig. 7(a). The element size has some influence on the prediction of fracture initiation as well as the connection capacity. The ultimate strength will increase 3.5% and decrease 1.4% for the models with 8-mm and 3-mm element size, respectively, when compared with the 5-mm one. It is because the fracture criterion is assumed to be active upon one integration location of an element [23], and the highly stress gradient around the connecting area causes significant difference for stress/strain values in a small distance apart from the weld toe. Furthermore, there is no convergence problem in simulation using ABAQUS/Explicit [23]. Despite this, under consideration of computational efficiency and the aspect ratio of elements, the element size of 5 mm around connecting area was adopted. The element aspect ratio is set as 1(length): 1(width): 1(depth) as possible near the connecting area. Therefore, through the tube-wall thickness, in the case of tube-wall thickness less than 5 mm, the element number was two, while for other cases it was three. The total number of elements was approximately 53,000 for the concrete part and 60,000 for the plate-to-CHS connection part respectively.

The loading areas in the FE models for parametric study were determined in accordance with those in the test specimens. The typical finite element mesh of plate-to-concrete-filled CHS connections under each loading condition is shown in Fig. 6.

Both directly speeding up the load applied on the models and using Mass Scaling Factor (MSF) will attain an equivalent effect on speeding up the time of simulation, where the former will reduce the number of increments required and the later will increase stable time increments. Since ABAQUS/Explicit, using explicit dynamics analysis procedure, will not check the calculation accuracy for each increment, the stable increment should be small enough to ensure the simulation accuracy. Large speed of simulation will cause extreme error in the results as shown in Fig. 7(b). Furthermore, mass scaling is attractive because it can be used in rate-dependent problems, but it must be used with care to ensure that the inertia forces do not dominate and change the solution [23]. Therefore the methodology of fixed mass scaling factor for computational cost control which is preferred in quasi-static analysis [23] was employed in this investigation. The sensitivity study on MSF values is presented in Figs. 7(b) and 7(c). Large MSF, i.e. 10^{11} and 10^{10}, will cause significant "vibration" in the whole simulation process and therefore leading to an extreme error in the result. Furthermore, due to the acceleration of loading process and the dynamic effects caused, the fracture prediction become earlier for the larger MSFs, i.e. 10^8 10^{10} and 10^{11}. The ratio of all kinetic energy (ALLIK) to all internal energy (ALLIE) was also used as an index to evaluate the stability of whole simulation procedure and the suitability of the MSF values in FE models. As suggested by ABAQUS [23], the ratio should not excess a small fraction value in the quasi-static simulation. Fig. 7(c) presents the history of ALLIK-to-ALLIE ratio throughout the whole simulation process for the models with MSFs to be 10^4, 10^6 and 10^8, all of which possess an extremely low value during the whole loading process except for the very beginning. Fig. 7(c) also indicates MSF values of 10^4 and 10^6 can achieve a stable simulation process with the maximum ratio less than 5%. The value of 10^6 was used after comparison analyses between models with MSF values of 10^4, 10^6, 10^8 10^{10} and 10^{11}. It can help FE models to achieve a satisfactory balance between accuracy and computational efficiency.

For the concrete constitutive model, the concrete-damaged plasticity model in ABAQUS (2010) was adopted herein. The constant values of 30°, 0.1, 1.16, 0.667 and 0.00025 [24,25] were adopted for dilation angle (Φ_s), flow potential eccentricity (e_{con}), ratio of the compressive strength under biaxial loading to uniaxial compressive strength (f_{bo}/f_{co}), the ratio of the second stress invariant on the tensile meridian to that on the compressive meridian (K_c), and viscosity parameter (μ), respectively. The sensitivity study on the parameters, Φ_s, f_{bo}/f_{co} and K_c, were conducted as shown in Fig. 8, while the parameters, e_{con} and μ, had no significant influence on prediction accuracy [26]. The default value of flow potential eccentricity e_{con}, 0.1[23], was adopted, and a small value, 0.00025 [25], was set for viscosity parameter μ. Fig. 8 shows the parameters Φ_s and f_{bo}/f_{co} have little effect on load-deformation curves, while the connection stiffness increases with K_c decreasing after 2-mm-chord-wall deformation developed.

The uniaxial compressive stress-strain relationship was defined using the equations suggested by Liang *et al*. [27], and the elastic modulus and Poison's ratio were taken as $4700\sqrt{f_c}$ [28] and 0.2 [29], respectively. The tensile behaviour of concrete was modeled by the fracture energy based method suggested by CEB-FIP Model Code 2010 [30]. The hard contact model in the normal direction and Coulomb friction model with a friction coefficient (μ) of 0.6 [24] in the tangential direction were used to simulate the interaction property between inside chord-face and its inner concrete. For the steel constitutive model, the plasticity properties were determined by the true stress-strain curves calibrated from the tensile coupon test, the von Mises yield criterion, associated flow rule and isotropic strain hardening. The fillet weld material was taken to be the same as the chord since it was designed to be equal strength with the parent metal. Furthermore by adopting the user subroutine program into FE models using ABAQUS/Explicit [23], the fracture failure of steel material was defined using the modified Mohr-Coulomb criterion (MMC) [31]. The effects of different stress states, including the first stress invariant and the second and third deviatoric stress invariants, on the facture initiation and propagation are considered base on the stress triaxiality and Lode angle parameter. Both initial fracture crack and its propagation have been successfully predicted on concrete-filled CHS connections under tensile loading and in-plane bending, where the chord-wall failed at shear-dominated fracture under the low stress triaxiality [25,32]. The detailed approach for derivation of MMC parameters and their sensitivity analyses can be found in the Ref. [25]. In total four parameters of A, n, c_1 and c_2 should be calibrated from material tests. Two material strain hardening parameters, A and n, were determined by calibrating from true stress-strain curve fitting of the Hollomon's power law [33], whilst the "internal friction" parameter c_1 and maximum shear resistance parameter c_2 were derived from test results by Bai [34] and Machinery's Handbook [35] respectively. The parameter values of the MMC criterion adopted in this study are shown in Table 3.

3.2. Verification

With an aim of verifying the applicability and reliability of the developed FE models, the ultimate loads obtained from FEA are compared with the test results in both Table 1 and Fig. 5. As indicated before, due to the rapid development of the fracture cracks along the weld-toe, the loads dropped dramatically once a throughout fracture crack (i.e. punching shear fracture of the tube-wall) formed. The ultimate bearing capacities of the specimens in the FE models were determined at the occurrence of the first failure element or elements which also coincided with the peak value in the load-deformation curves in Figs. 4 and 9. Fig. 3 shows there is a good correlation for both failure mode and crack propagation between tests and numerical simulations under each loading condition. Furthermore the load-deformation response of the FE models match well with the experimental results on initial stiffness, peak load and ductility for all test specimens, as shown in Fig. 4 (excluding the repeated connections). The chord-wall deformations in FEA results were attained in the same way as the experimental ones at the same locations. The element nodal or interpolated nodal displacements in the normal direction were used instead of LVDT readings. All above comparisons between tests and FEA with respect to the failure modes, the chord tube wall fracture location, the ultimate loads at the failure point and overall load-deformation behaviour, show a good correlation. It demonstrates that adopted FE modeling methodology adequately predicts the general behaviour of the test specimens and therefore are deemed reliable and suitable for using in a parametric study.

Based on the validated finite element models, a total of 336 FE models of connection under three types of loading condition, including axial tension (138), eccentric tension (60) and in-plane bending (138), was established with geometrical configurations and material properties varied each and specified in the following sections. The chord length and plate height were kept constant as aforementioned and all other details such as the boundary conditions, interaction between steel and concrete and loading speed kept the same with that verified benchmarked FE models, if not specially mentioned. Table 3 also shows the steel materials used in parametric study, whilst the material property of concrete keeps invariant as the verified benchmarked FE models.

4. Analysis and discussions

4.1. Limit state for longitudinal plate-to-concrete-filled CHS connections

Less than 3%*D* localized chord-wall deformations and connection capacities governed by punching shear dominated fracture failure were observed in previous experimental studies [6,10]. To determine the limit state, either the connection capacity under the deformation limit or 1.5 times of serviceability deformation limit suggested by previous research [36,37] were compared with the experimental ultimate strengths in Xu *et al*. [10]. It is demonstrated that the capacity of those test connections is governed by the ultimate strength rather than a deformation limit. However this conclusion is limited to the geometry of experimental specimens. With an aim of deriving a more widely appreciable conclusion for further development of design equations, the scope of experimental connection specimens were extended by finite element parametric study. The load-deformation curves from FE models were determined by the displacement difference between point B and B_1 (10 mm away for the weld toe) versus measured load multiplied its force arm (M_{EXP} = F_{EXP} × 790 mm). The ultimate capacities were determined as the minimum of two defining limit states: 1) the maximum load and 2) the load at a deformation of 3%*D*. For all FE models, the connection capacities were governed by the peak load when punching shear failure occurred, which also confirmed the former experimental conclusion that the only ultimate strength limit at punching shear dominated fracture failure would govern the connection capacity when the strength of both branches (plates, bolts and braces) and main members (chords) were adequate. The typical FEA load-deformation curves are shown in Fig. 9.

4.2. Distribution of punching shear stress

From the experimental observations [6,10] and the numerical analysis in the former sections, the shear stress profiles on the failure face become a crucial aspect in proposing a reliable and accurate design method. However the inaccessibility of shear stress on a fracture failure face by strain gauges or digital image correlation technology limits the experimental development of the fracture mechanism based design method from test results. Therefore the FEA have been adopted to investigate the shear stress distribution on the failure face in this paper.

(a) Axial tension series

The uniformity of shear stress distribution of a connection under axial tension is usually affected by the ratio (η_b) of the length of the loading area (l_{load}) to the plate (l_b). The ratio can be transformed to an expression, as shown in Eq. (1) with an angle (θ) when the plate length and height were given, as shown in Fig. 10(a).

$$\eta_b = \frac{l_{load}}{l_b} = 1 - 2\frac{h_b}{l_b}\tan\theta \tag{1}$$

The varied parameters include: length ratios η_b (0.56, 0.40, 0.24, and 0.04), chord diameter D (240, 300, and 400 mm), chord-wall thickness t (3, 4, 5, and 6 mm) and plate thickness t_b (8, 10, 12, and 15 mm). To investigate the shear stress distribution on the chord-wall in different cases of η_b especially for small values, the capacity of the gusset plate will be ensured not to fail before the chord-wall fracture. Typical shear stress distributions of connections (within the plate-length region) with different length ratios η_b are presented in Fig. 10(b). The location variable for shear stress profile in the longitudinal direction along the failure face is normalized as expressed in terms of $\overline{L_b}$, as shown in Fig. 10(a). It is shown that stress distribution curves are almost uniform and closed with each other located at a similar stress level with the same contour profile. This indicates that the length ratio η_b has limited effect. It can be attributed to the inner concrete which prevents the inward deformation of chord-wall and provides additional radius stiffness to a chord member, resulting the evenly and locally developed chord-wall deformation along the connecting area. Therefore the tensile load can be transformed from the gusset plate uniformly before the chord-wall reaches the punching shear fracture, providing that the capacity of the plate is ensured. Based on the FEA results, it is reasonable to exclude the effect of loading area and assume it to be invariable when the plate length varies in the subsequent parametric study.

From the parametric study, the shear stress distribution can be conservatively described as Eq. (2) on the assumption that the distribution is uniform along both longitudinal and transvers direction of plate. Based on the FE models with the ranges for each parameters of D, t, l_b, t_b to be 240~400mm, 3~6mm, 300~600mm and 8~15mm, respectively, the value of k_{AX}, as shown in Fig. 11 can be approximately determined as 0.85.

$$\begin{cases} f_{\tau,\mathrm{AX}}\left(\overline{L_{\mathrm{b}}}\right)= f_{\mathrm{v,min}} = k_{\mathrm{AX}} f_{\mathrm{v,max}} & \text{Longitudinal side} \\ f_{\tau,\mathrm{AX}}\left(\overline{T_{b}}\right)= f_{\mathrm{v,max}} & \text{Transverse side} \end{cases} \tag{2}$$

where $f_{v,max}$ and $f_{v,min}$ are the maximum and minimum shear stresses on the punching shear face; k_{AX} is the ratio of $f_{v,min}$ to $f_{v,max}$; $\overline{L_b}$ is a relative position parameter $(\Delta l_b)/l_b$ defined in Fig. 10(a); and $\overline{T_b}$ is a relative position parameter $(\Delta t_b)/t_b$ defined in the same way as $\overline{L_b}$.

(b) In-plane bending series

Typical shear stress profiles on the failure face for connections T-240-4-500-12-IB and T-300-4-500-12-IB are plotted as symbol-line curves in Figs. 12(b) and (c). Limited variation of stress profiles was observed from parametric study when geometrical parameters of t_b, D and t varied, as shown in Figs. 13(a)-(c). It is also noted that the neutral axis moves to the compressive side for the local bearing of its inner concrete. The longitudinal shear stress distribution at maximum load step therefore can be proposed and expressed as Eq. (3) in which a parabolic function for the compressive side and a double dogleg function for the tensile side are employed.

$$f_{\tau,\mathrm{IB}}\left(\overline{L_{\mathrm{b}}}\right)= \begin{cases} \dfrac{\left|f_{\mathrm{v,cmax}}\right|}{\left(n_1-n_0\right)^2}\left(\overline{L_{\mathrm{b}}}-n_0\right)^2-\left|f_{\mathrm{v,cmax}}\right| & 0\le \overline{L_{\mathrm{b}}}<n_1 \\ \dfrac{0.55 f_{\mathrm{v,tmax}}}{n_2-n_1}\overline{L_{\mathrm{b}}}-\dfrac{0.55 f_{\mathrm{v,tmax}} n_1}{n_2-n_1} & n_1\le \overline{L_{\mathrm{b}}}<n_2 \\ \dfrac{0.45 f_{\mathrm{v,tmax}}}{1-n_2}\overline{L_{\mathrm{b}}}+\dfrac{0.55 f_{\mathrm{v,tmax}}-f_{\mathrm{v,tmax}} n_2}{1-n_2} & n_2\le \overline{L_{\mathrm{b}}}<1 \end{cases} \tag{3}$$

where $f_{v,cmax}$ and $f_{v,tmax}$ are the maximum shear stresses on the punching shear face at the compression and tensile sides respectively; $\overline{L_b}$ is relative length $(\Delta l_b)/l_b$ shown in Fig. 10(a); n_1 is normalized location parameter for of the neutral axis; n_0 and n_2 are normalized location parameters for the maximum stress point at compressive side and the corner point of double dogleg curve at tensile side respectively. The normalized parameters of n_0, n_1 and n_2 are also shown in Fig. 12(a).

The parametric study was conducted using the verified FE models to investigate the constants of n_0, n_1 and n_2 for a specified connection, as shown in Fig. 14. The study consisted of connections with geometrical dimensions ranging from three values of chord diameter D, 180~300 mm, three values of chord thickness t, 3~5 mm, four values of plate thickness t_b, 8~15 mm, and three values of plate length l_b, 340~600 mm. It is shown that the values of n_0, n_1 and n_2 ranges from 0.1 to 0.2, 0.29 to 0.39, and 0.42 to 0.52, respectively. The average values of each range, $n_0 = 0.15$, $n_1 = 0.34$, and $n_2 = 0.47$, are recommended in this study. Based on these values, the location of $f_{v,cmax}$, and neutral axis can be then determined as shown in Fig. 12(a). Therefore, the general shear stress profile on the failure face for a longitudinal plate-to-concrete-filled CHS connection under in-plane bending can be determined by substituting the recommended values of n_0, n_1 and n_2 into Eq. (3). Figs. 12(b) and (c) show the curves predicted by the proposed equations match well with the FEA results.

(c) Effects of load eccentricity

A series of FE models with four values of relative eccentricity (e/l_b = 0.00, 0.10, 0.17, 0.25) but with the same geometrical configuration was carried out to investigate the effect of load eccentricity on the shear stress distributions. The shear stress profiles on fracture failure face for FE models with different eccentricities are shown in Fig. 13(d). The shear stress far from the loading region became lower even to be "negative" (change of the shear stress direction) with the increment of the load eccentricity, while the maximum stresses at tensile side for all connections remained almost the same. It also indicated that the eccentric tension could be assumed as an axial tension and an in-plane bending causing by corresponding load eccentricity.

5. Design methods

5.1. Design philosophy

In this study, the connection design method is based on a limit-state design format known as Load and Resistance Factor Design (LRFD). The connection capacity should be determined by the lower one of (a) the ultimate strength and (b) the load corresponding to a deformation limit, which is recommended by CIDECT-1. However, the only limit state of punching shear dominated fracture at tube wall for longitudinal plate-to-concrete-filled CHS connections was observed and confirmed when compared the ultimate strength with the load corresponding to the well-accepted deformation limit of 3% chord diameter (D) criteriion. Therefore, only the punching shear failure mode is considered for connections under axial tension, eccentric tension and in-plane bending.

Figs. 10(a) and 12(a) show the analytical models for the connections under axial tension and in-plane bending respectively. The proposed equations, Eqs. (2) and (3) are employed to describe the shear stress distributions. For the case of axial tension, the external force is assumed to be resisted only by chord-wall; whilst for the case of in-plane bending, both chord-wall and its inner concrete work together to resist the external moment.

5.2. Position of resultant force point for the connections under in-plane bending

(a) Compressive side

Both shear stress on the chord-wall failure face and local compressive stress in the inner concrete participated into the sectional resistance for longitudinal plate-to-concrete-filled CHS connection observed from numerical results. Figs. 15(a) and (b) show that the distributions of von Mises stress and stress component (S22) perpendicular to the longitudinal chord axis, in the concrete for the FE model T-240-4-500-12-IB, respectively. The local compressive stress achieved the peak value approximately at the position of $0.1l_b$ from the compressive side as shown in Fig. 15(a) in the front view and exhibited a good symmetry with the central axial as indicated in Fig. 15(b). Derived by integral of Eq. (3), the value of resistance force afforded by tube-wall on the tensile side is approximately ten times of it on the compressive side. Furthermore, from the rule of force equilibrium on both sides, the resistance force provided by local bearing of the inner concrete reaches almost 90% of it on the tension side and nine times of it afforded by tube-wall on the compression side. Therefore, it is reasonable to assume the resultant force point ($O_{c,IB}$) is located on the $0.1l_b$ at the compressive side for calculation simplification. The resultant force point, $O_{c,IB}$, is also pointed in Fig. 12(a).

(b) Tensile side

The sectional tensile resistance was provided by the chord-wall only. Using Eq. (3), the value of $Z_{t,IB}$ can be calculated from Eq. (4). The resultant force point ($O_{t,IB}$) on the tensle side and other relative information are presented in Fig. 12(a).

$$Z_{\mathrm{t,IB}} = \frac{\iint_{\Sigma 1} f_{\tau,\mathrm{IB}} z_{\mathrm{t,IB}} \mathrm{d}S_1}{\iint_{\Sigma 1} f_{\tau,\mathrm{IB}} \mathrm{d}S_1} \approx 0.394\, l_{\mathrm{b}} \tag{4}$$

where $Z_{t,IB}$ is the vertical distance from $O_{t,IB}$ to the neutral axis; S_1 is a single longitudinal failure face along the chord axes; and $z_{t,IB}$ is the vertical distance from the calculation point to the neutral axis; and l_b is the longitudinal length of plate.

(c) Internal lever arm of the section

The internal lever arm (Z_{IB}) of the moment section is the sum of $Z_{c,IB}$ (= $0.35l_b$ -$0.1l_b$) and $Z_{t,IB}$, which is determined as follows:

$$Z_{\mathrm{IB}} = Z_{\mathrm{c,IB}} + Z_{\mathrm{t,IB}} = (0.35 - 0.1)l_{\mathrm{b}} + 0.394 l_{\mathrm{b}} = 0.644 l_{\mathrm{b}} \tag{5}$$

5.3. Maximum shear stress

The punching shear dominated fracture has been shown to govern the mechanical behaviour of the longitudinal plate-to-concrete-filled CHS connections. For most cases, the load corresponding to the first throughout fracture crack in tests and the first failed element in FEA indicates the punching shear capacity of a connection. Despite the connections are failed due to the shear failure of the chord-wall material, the maximum shear stress ($f_{v,max}$ or $f_{v,tmax}$) in the failing element is in fact lower than the material ultimate shear strength, $f_{u,v}$. It is because that the element achieves its maximum shear stress ($f_{v,max}$ or $f_{v,tmax}$) when it fails under a triaxial stress state also corresponding to an equivalent plastic strain on the fracture failure surface; while the ultimate shear strength for steel material is determined at the pure shear stress state. Therefore the parametric study with respect to different geometrical configurations, material properties and loading conditions was conducted to study the ratio of the maximum shear stress, $f_{v,max}$ or $f_{v,tmax}$, to material shear stress, $f_{u,v}$, at each loading condition. Figs. 16(a) and (b) show the FEA results that the ratios of $f_{v,max}$ / $f_{u,v}$ and $f_{v,tmax}$/ $f_{u,v}$ are approximately determined to be 0.70 and 0.72, respectively.

5.4. Simplified analytical models and design equations

(a) Axial tension series

The analytical model for longitudinal plate-to-concrete-filled CHS connection under axial tension is presented in Fig. 10(a). The uniform shear stress distribution is assumed on the both side and end failure faces with the amplitude equal to $k_{AX}f_{v,max}$ and $f_{v,max}$, respectively. The ultimate strength at the punching shear limit state for connections under axial tension is considered as the total shear force on the whole failure face including both side and end ones, but excluding the effect of weld width. As aforementioned parametric study, the value of $f_{v,max}$ is taken as 70 % of the ultimate shear strength $f_{u,v}$, which is $f_{v,max}$= 0.70 $f_{u,v}$ = 0.70 × 0.75F_u [35]. Thus the ultimate tensile strength can be calculated from Eq. (6):

$$\begin{aligned} F_{u,AX} &= 2\times(t\,l_b k_{AX}\,f_{v,max} + t\,t_b\,f_{v,max}) \\ &= \left(0.9 l_b + 1.1 t_b\right) t\,F_u \end{aligned} \tag{6}$$

Where $F_{u,AX}$ is the ultimate strength; k_{AX} is the ratio of $f_{v,min}$ to $f_{v,max}$; l_b is the plate length; t_b is the plate thickness; t is the chord-wall thickness; and F_u is the steel ultimate tensile strength for the chord.

(b) In-plane bending series

The ultimate strength on the punching shear limit state for in-plane bending connections is the whole moment resistance of a fracture face including both side and end ones. The sectional moment resistance is considered as the sum of the shear force multiplying its vertical distance to the neutral axis on the failure face. The shear strength profile is described as Eq. (3) for a single longitudinal side failure face, whilst for a single end failure face the uniform shear stress profile with the amplitude equal to $f_{v,tmax}$ is employed in the analytical model which conservatively excludes the effects of weld width. The specified analytical model is shown in Fig. 12(a). The ultimate moment strength can be proposed as shown in Eq. (7) is:

$$M_{u,IB} = 2\iint_{\Sigma 1} f_{\tau,IB} z_{IB} dS_1 + F_{V2,IB} \times (l_b - 0.1 l_b) = 2F_{V1,IB} \times Z_{IB} + 0.9F_{V2,IB} \times l_b \tag{7}$$

where $M_{u,IB}$ is the ultimate in-plane bending strength; $f_{\tau,IB}$ is the distribution function of shear stress on single side failure face; z_{IB} is the resistance arm from the calculated point to the compressive force resultant point; $F_{V1,IB}$ and $F_{V2,IB}$ are the sum of shear stress on the tensile side of the single side and end failure face, respectively; Z_{IB} is the internal lever arm; and l_b is the plate length.

The value of $F_{V1,IB}$ can be computed by an integral of the shear stress and its area S_1 on the tensile side, Substituting Eq. (3), the $F_{V1,IB}$ can ultimately be written as Eq. (8).

$$F_{V1,IB} = \iint_{\Sigma 1} f_{\tau,IB} dS_1 \approx 0.447 l_b\, t\, f_{v,tmax} \tag{8}$$

$$F_{V2,IB} = t_b\, t\, f_{v,tmax} \tag{9}$$

where $f_{v,tmax}$ is equal to 0.72 $f_{u,v}$ = 0.72 × 0.75F_u [35].

Then, by substituting Eqs. (5), (8) and (9), Eq. (7) can be rewritten as Eq. (10).

$$M_{u,IB} = (0.31 l_b + 0.49 t_b) l_b\, t\, F_u \tag{10}$$

where $M_{u,IB}$ is the ultimate in-plane bending strength; l_b is the plate length; t_b is the plate thickness; t is the chord-wall thickness; and F_u is the steel ultimate tensile strength for the chord.

(c) Eccentric tension series

The linear relationship between the strengths of axial tension and in-plane bending is adopted in CIDECT-1 for the design of punching shear. This is also verified from FE results as a low bound of the 95% prediction band, as shown in the Fig. 17. Therefore it is recommended in this study. So the ultimate strength at the punching shear failure mode is shown in Eq. (11).

$$\frac{F_{u,E}}{F_{u,AX}} + \frac{eF_{u,E}}{M_{u,IB}} \le 1.0, \quad \frac{F_{u,E}}{F_{u,AX}} > 0 \text{ and } \frac{eF_{u,E}}{M_{u,IB}} > 0 \tag{11}$$

where $F_{u,AX}$ is the axial strength calculated using Eq. (6); $M_{u,IB}$ is the design moment strength calculated using Eq. (10); e is the load eccentricity; and $F_{u,E}$ is the design strength for a connection under eccentric tension.

5.5. Summary and comparison between results of design equations, test and finite element analysis

The proposed ultimate strengths design equations for longitudinal plate-to-concrete-filled CHS connection under three investigated loads as well as their applicable ranges are presented in Table 4. The results of the proposed design equations under different loading conditions are compared with the results of both tests and FEA, as presented in Table 1 and Tables 5~7 respectively. It is shown that the design strengths are slightly conservative since the effect of the weld width is neglected. Meanwhile the design equations were modified by incorporating weld width to further evaluate their applicability and accuracy. The results, $F_{u,weld}$ and $M_{u,weld}$, are compared with FEA with the mean values of F_{u,AX_weld} /F_{FEA}, M_{u_weld}/M_{FEA} and F_{u,E_weld} /F_{FEA} being 0.97 (Table 5), 1.03 (Table 6) and 1.0 (Table 7), respectively, which exhibit a good correlation. Nevertheless Eqs. (6), (10) and (11) are still recommended to be the design equations since the weld width is difficult to be precisely considered in practical design.

6. Conclusions

The governing limit states, the shear stress profiles on the failure face, and the connection capacity design equations based on the failure mode for longitudinal plate-to-concrete-filled CHS connections under axial tension, eccentric tension and in-plane bending were investigated by finite element analysis. MMC fracture criterion was incorporated into the finite element model. It is shown that the governing limit state is the ultimate strength of punching shear failure instead of deformation limit of 3% chord diameter (D). It is attributed that the infilled concrete prevents the chord-wall inward deformation which significantly improves the stiffness of the chord face. Through the parametric investigation, the uniformity distribution function for the case of axial tension and the combined paraboloid and polygonal functions for the case of in-plane bending were proposed to describe the shear stress profile. Different analytical models on the concept of sectional resistance for the punching shearing failure were established and used to elaborate the fracture behaviour of connections under three investigated loads. Finally, three design equations for longitudinal plate-to-concrete-filled CHS connection were proposed and compared with both tests and FEA results. The results indicated that design predictions agreed well with both experimental and FEA results.

Acknowledgments

The research work described in this paper was supported by Research project from Science and Technology Department of Zhejiang Province (2015C33005). The first and third authors are also grateful for the support from the Chinese National Engineering Research Centre for Steel Construction (Hong Kong Branch).

References

[1] O'Shea MD, and Bridge RQ. Design of thin-walled concrete filled steel tubes. J Struct Eng ASCE 2000; 10.1061/(ASCE)0733-9445(2000)126:11(1295), 1295-1303.

[2] Uy, B. Local and postlocal buckling of fabricated steel and composite cross sections. J Struct Eng ASCE 2001; 10.1061/(ASCE)0733-9445(2001)127:6(666), 666–677.

[3] Bradford MA, Loh HY, Uy B. Slenderness limits for filled circular steel tubes. J Constr Steel Res 2002; 58(2), 243-252.

[4] Kosteski N, Packer JA. Longitudinal plate and through plate-to-hollow structural section welded connections. J Struct Eng ASCE 2003; 129(4), 478-486.

[5] Kosteski N. Branch plate-to-rectangular hollow structural section connections. Ph.D. thesis, University of Toronto, Toronto, Ontario, Canada; 2001.

[6] Voth AP. Branch plate-to-circular hollow structural section connections. Ph.D. thesis, University of Toronto, Toronto, Ontario, Canada; 2011.

[7] Lee MMK, Llewelyn-Parry A. Strength of ring-stiffened tubular T-joints in offshore structure: a numerical parametric study. J Constr Steel Res 1999; 51(3), 239-264.

[8] Lee MMK, Llewelyn-Parry A. Offshore tubular T-joints reinforced with internal plain annular ring stiffeners. J Struct Eng ASCE 2004; 130(6), 942-951.

[9] Willibald S. The static strength of ring-stiffened tubular T-and Y-joints. In: Proceedings of 9th Int. Symp. On Tubular Structures, A.A. Balkema Dusseldorf, 2001; 581-588.

[10] Xu F, Chen J, Jin WL. Experimental investigation of concrete-filled steel tubular longitudinal gusset plate connections. J Constr Steel Res 2016; 124, 163-172.

[11] Wardenier J, Kurobane Y, Packer JA, van der Vegte GJ, Zhao XL. Design guide for circular hollow section (CHS) joints under predominantly static loading, 2nd Ed., CIDECT-1. Comité International pour le Développement et l'Étude de la Construction Tubulaire, LSS Verlag, Germany, 2008.

[12] Davies G, Packer JA. Predicting the strength of branch RHS connections for punching shear. Can J Civ Eng 1982; 9(3), 458-467.

[13] Dawe JL, Guravich SJ. Branch plate to reinforced HSS connections in tension and compression. Can J Civ Eng 1993; 20(4), 631-641.

[14] Cao JJ, Packer JA, Kosteski N. Design guidelines for longitudinal plate to HSS connections. J Struct Eng 1998; 124(7), 784-791.

[15] Cao JJ, Packer JA, Kosteski N. Determination of connection strength between longitudinal plates and RHS columns. J Constr Steel Res 1998; 1(46), 243-244.

[16] Voth AP, Packer JA. Branch plate-to-circular hollow structural section connections. I:

Experimental investigation and finite-element modeling. J Struct Eng ASCE 2012; 138(8), 995-1006.

[17] Voth AP, Packer JA. Branch plate-to-circular hollow structural section connections. II: X-type parametric numerical study and design. J Struct Eng ASCE 2012; 138(8), 1007-1018.

[18] Voth AP, Packer JA. Numerical study and design of T-type branch plate-to-circular hollow section connections. Eng Struct 2012; 41, 477-489.

[19] Packer JA, Wardenier J, Zhao XL, van de Vegte GJ, Kurobane Y. Design guide for rectangular hollow section (RHS) joints under predominantly static loading, 2nd Ed., CIDECT-3. Comité International pour le Développement et l'Étude de la Construction Tubulaire, Verlag TÜV Rheinland. Cologne, Germany; 2009.

[20] API RP2A-WSD. Recommended practice for planning, designing and constructing fixed offshore platforms, 23nd. Washington D.C., USA: American Petroleum Institute (API), 23nd, 2014.

[21] ANSI/AISC 360-10. Specification for structural steel buildings. Chicago, USA: America Institute of Steel Construction (AISC); 2010.

[22] *ABAQUS 6.10* [Computer software]. Dassault systemes, Waltham, MA, USA; 2010.

[23] Hibbitt HD, Karlsson BI, Sorensen P. ABAQUS standard user's manual, Ver.6.10, USA; 2010.

[24] Han, LH, Yao, GH, Tao, Z. Performance of concrete-filled thin-walled steel tubes under pure torsion. Thin-Walled Struct 2007; 45(1), 24-36.

[25] Xu, F, Chen, J, Chan, TM. Mechanical behaviour of concrete-filled CHS connections subjected to in-plane bending. Eng Struct 2017; 148, 101-112.

[26] Tao, Z, Wang, ZB, Yu, Q. Finite element modelling of concrete-filled steel stub columns under axial compression. J Constr Steel Res 2013; 89, 121-131.

[27] Liang, QQ, Fragomeni, S. Nonlinear analysis of circular concrete-filled steel tubular short columns under axial loading. J Constr Steel Res 2009; 65(12), 2186-2196.

[28] ACI (American Concrete Institute) Committee 318. Building Code Requirements for Structural Concrete (ACI 318-11) and Commentary (ACI 318R-11). Farmington Hills, MI: ACI; 2011.

[29] Hu HT, Huang CS, Wu MH, Wu YM. Nonlinear analysis of axially loaded concrete-filled tube columns with confinement effect. J Struct Eng ASCE 2003; 129(10): 1322-1329.

[30] FIP. CEB-FIP Model Code 2010-Final draft, Vol.1. Lausanne, Switzerland: federation internationale du béton; 2012.

[31] Bai, Y, Wierzbicki, T. Application of extended Mohr-Coulomb criterion to ductile fracture. Int J Fract 2010; 161(1), 1-20.

[32] Xu, F, Chen, J, Jin, WL. Punching shear failure of concrete-filled steel tubular CHS

connections. J Constr Steel Res 2016; 124, 113-121.
[33] Hollomon, JH. Tensile deformation. Trans AIME 1945; 12, 268-290.
[34] Bai, Y, Wierzbicki, T. A comparative study of three groups of ductile fracture loci in the 3D space. Eng Fract Mech 2015; 135, 147-167.
[35] John, MA. Franklin, DJ, Henry, HR. Guide to the Use of Tables and Formulas in Machinery's Handbook, 28th Ed. Industrial Press, New York; 2008.
[36] Lu, LH, De Winkel, GD, Yu, Y, Wardenier, J. Deformation limit for the ultimate strength of hollow section joints. In: Proceedings of 6th Int. Symp. on Tubular Structures, 1994; 341-347.
[37] Zhao, XL. Deformation limit and ultimate strength of welded T-joints in cold-formed RHS sections. J Constr Steel Res 2000; 53(2), 149-165.

Nomenclature

The following symbols are used in this paper:

A = parameters of material strain hardening;

c_1 = friction coefficient in Mohr-Coulomb model;

c_2 = shear stress resistance in Mohr-Coulomb model;

D = outer diameter of the chord member;

e = load eccentricity;

e_{con} = flow potential eccentricity in the concrete damaged plasticity model;

E_s = Young's modulus of steel;

E_c = Young's modulus of concrete;

f_c = concrete compressive design strength;

f_{cu} = concrete compressive cube strength;

$f_{u,v}$ = ultimate shear strength of steel;

$f_{v,max}$, $f_{v,min}$ = maximum and minimum shear stress on the punching shear face in the case of tension;

$f_{v,cmax}$, $f_{v,tmin}$ = maximum and minimum shear stress on the punching shear face at the compressive side face in the case of in-plane bending;

$f_{\tau,AX}$, $f_{\tau,IB}$ = shear stress distribution on the punching shear face;

F_{EXP}, F_{FEA} = ultimate strength obtained from tests and FEA;

$F_{u,AX}$, F_{u,AX_weld} = ultimate strength obtained from design equations in case for axial tension with and without the weld effect respectively;

$F_{u,E}$ and F_{u,E_weld} = ultimate strength obtained from design equations in case eccentric tension with and without the weld effect respectively;

F_y = yield strength of steel;

F_u = ultimate strength of steel;

$F_{V1,IB}$, $F_{V2,IB}$ = sum of shear stress on the tensile side for side and end failure face in case of in-plane bending;

k_{AX} = ratio of $f_{v,min}$ to $f_{v,max}$ in the case of axial tension;

K_c = the ratio of the second stress invariant on the tensile meridian to that on the compressive meridian in the concrete damaged plasticity model;

L = length of the chord;

$\overline{L_b}$ = position parameter defined in Fig. 10(a);

l_b = longitudinal length of plate;

l_{bp} = bolt-plate length;

h_b = plate height;

M_{EXP}, M_{FEA}, $M_{u,IB}$, M_{u_weld} = ultimate moment strength obtained from tests, FEA and proposed design equations (with and without the weld effect);

N = parameters of material strain hardening;

$O_{c,IB}$, $O_{t,IB}$ = the resultant point of tension and compressive side in the case of in-plane bending;

$\overline{T_b}$ = a relative position parameter $(\Delta t_b)/t_b$ defined in the same way as $\overline{L_b}$;

t = chord-wall thickness;

t_b = longitudinal plate thickness;

t_{bp} = bolt-plate thickness;

$Z_{c,IB}$, $Z_{t,IB}$ = distance from compressive and tensile resultant points to the neutral axis respectively;

Z_{IB} = internal lever arm of the moment section;

ε_f = elongation (tensile strain) after fracture based on a gauge length of 50 mm;

β = ratio of plate thickness to chord outer diameter;

η = ratio of plate longitudinal length to chord outer diameter;

γ = ratio of chord outer radius to chord thickness;

η_b = ratio of length of loading area to plate in the longitudinal direction;

θ = angle shown in Fig. 10(a);

τ = ratio of plate thickness to chord thickness;

n_0, n_1, n_2 = the position of $f_{v,cmax}$, neutral axis and $f_{v,tmax}$ in the shear stress profile in case of in-plane bending;

μ = viscosity parameter in the concrete damaged plasticity model;

f_{bo}, f_{co} = initial equibiaxial compressive yield stress and initial uniaxial compressive yield stress in the concrete damaged plasticity model;

Φ_s = dilation angle measured in the p-q plane in the concrete damaged plasticity model.

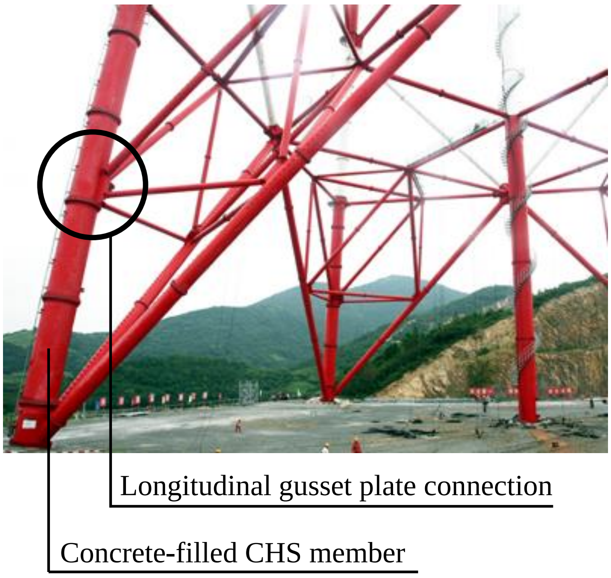

Fig. 1. Large-span transmission tower in China.

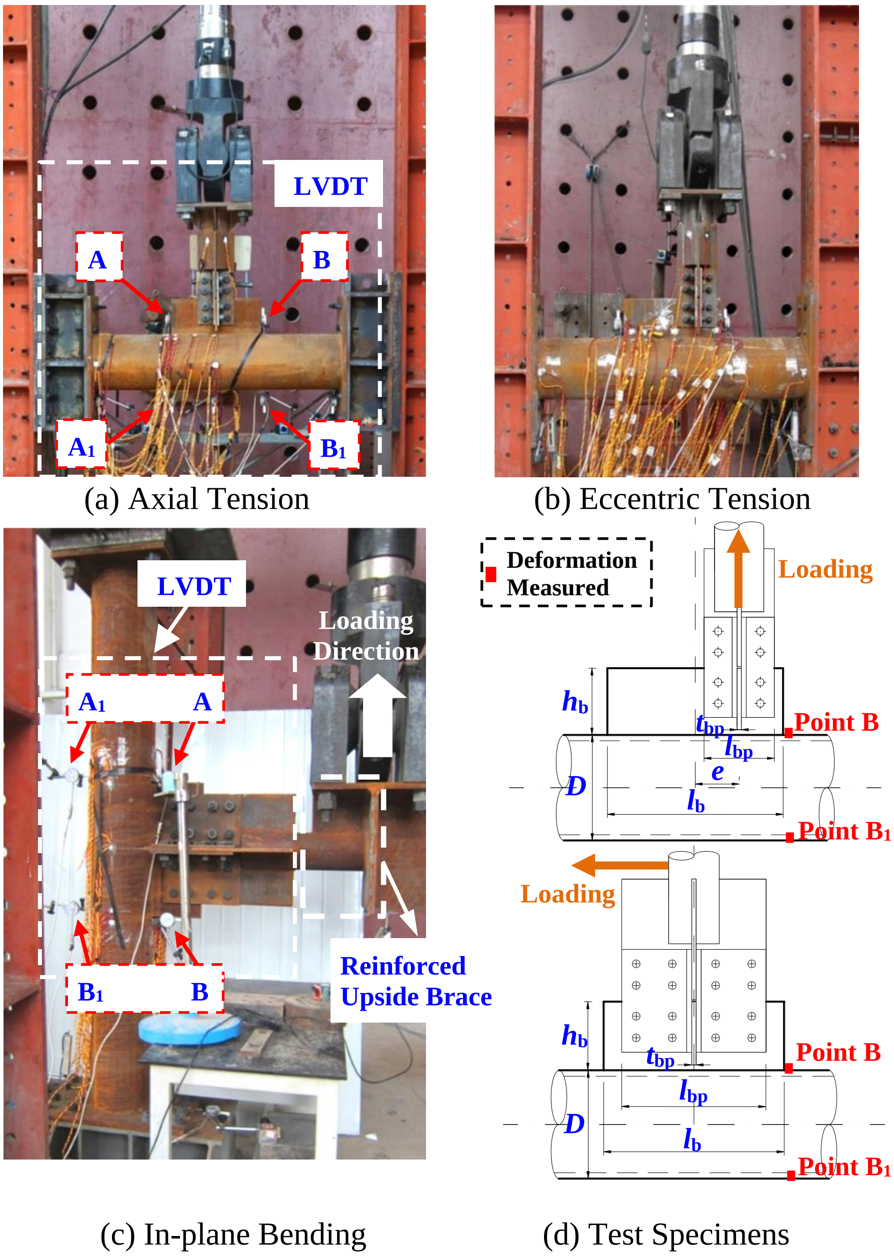

(a) Axial Tension (b) Eccentric Tension

(c) In-plane Bending (d) Test Specimens

Fig. 2. Test set-up [10] and test specimens. (Unit: mm)

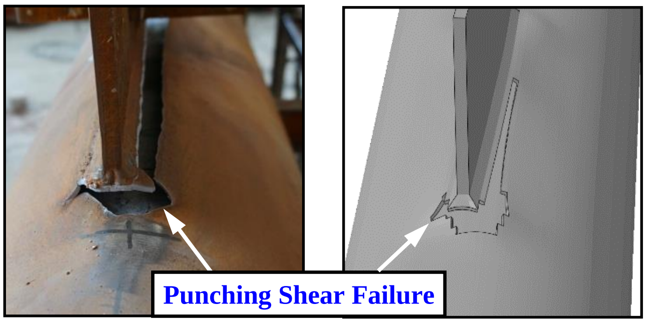

(a) T-300-4-AX

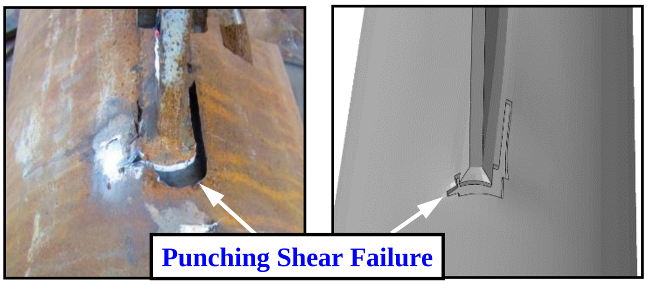

(b) T-300-4-E125

(c) T-300-4-IB

Fig. 3. Failure modes of test specimens (Left: experiment; right: FEA)

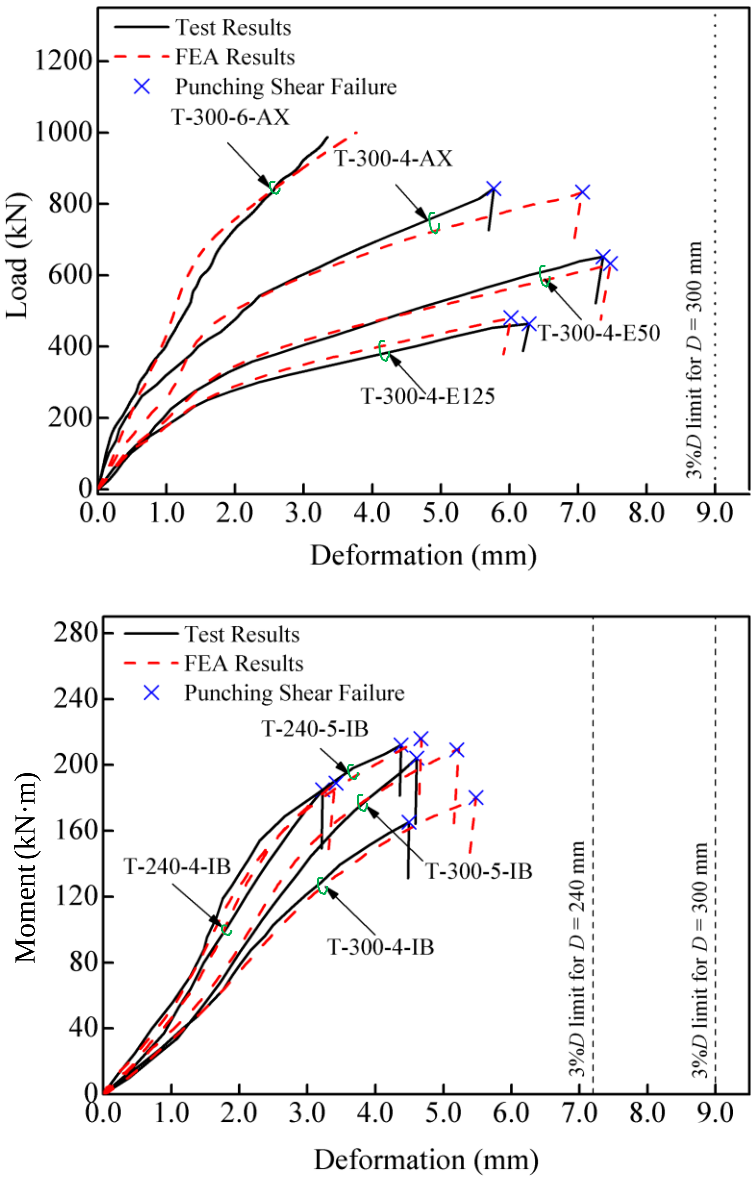

Fig. 4. Comparison of load-deformation and moment-deformation curves between test and FEA results

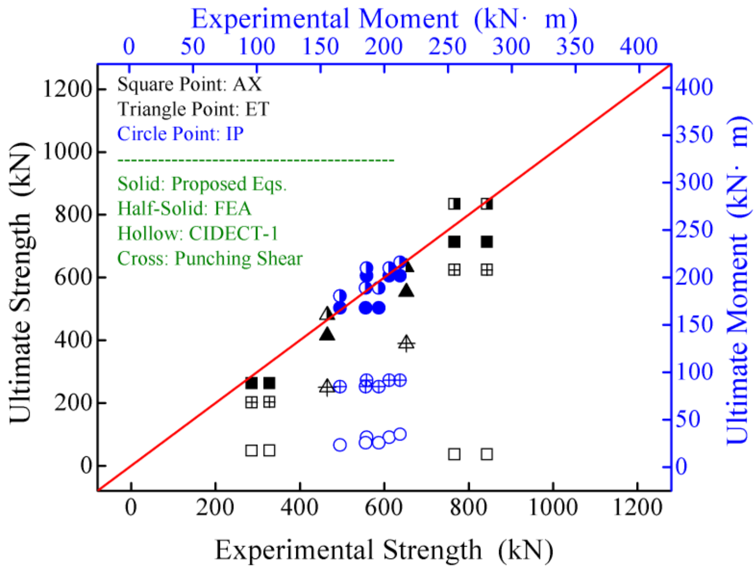

Fig. 5. Comparison of ultimate strength between test, FEA and calculated results (AX: axial tension; ET: eccentric tension; IP: in-plane bending)

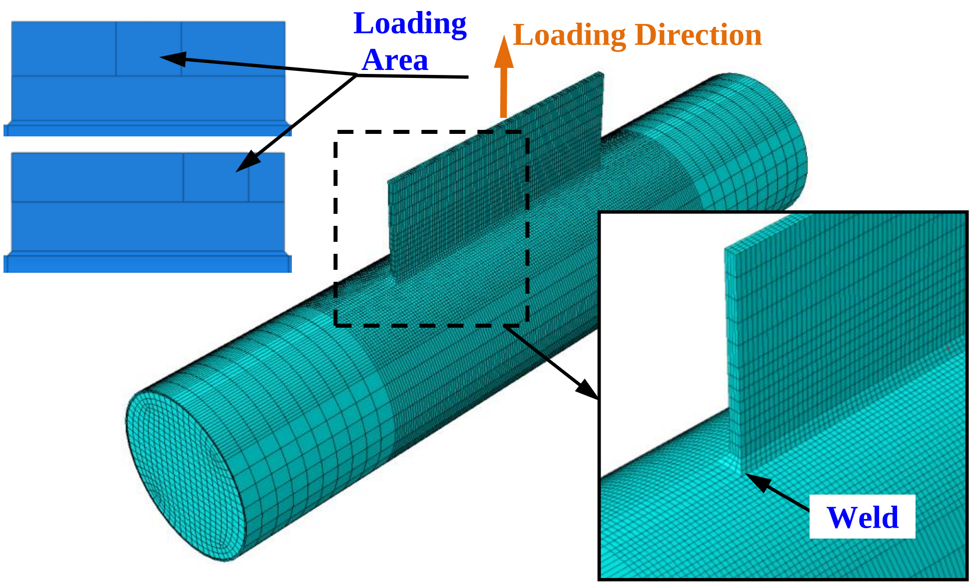

(a) Connection under Tension

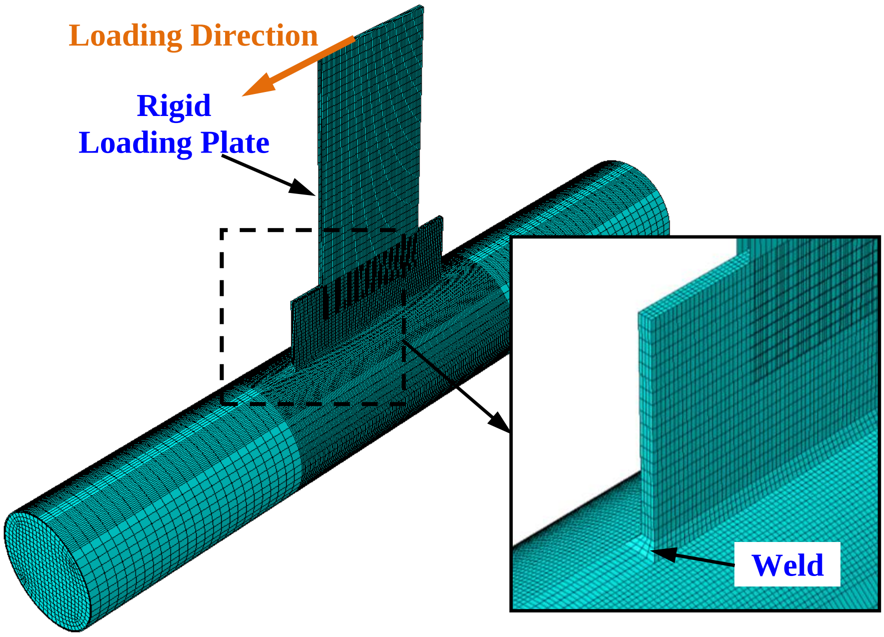

(b) Connection under in-plane bending

Fig. 6. Finite element model

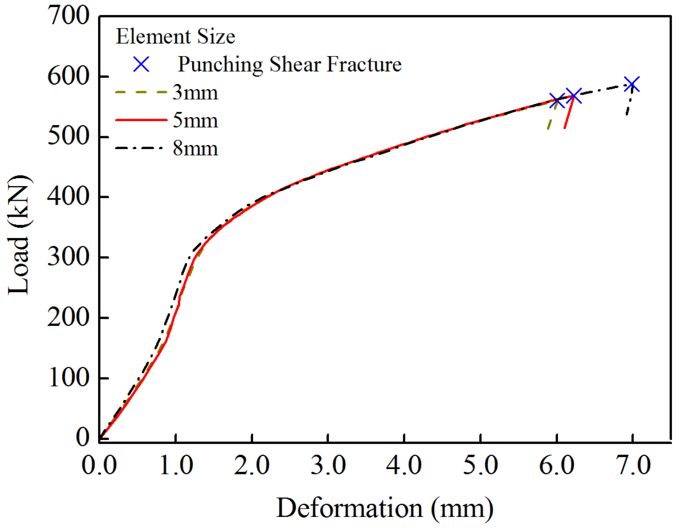

(a) Element size around the connecting area

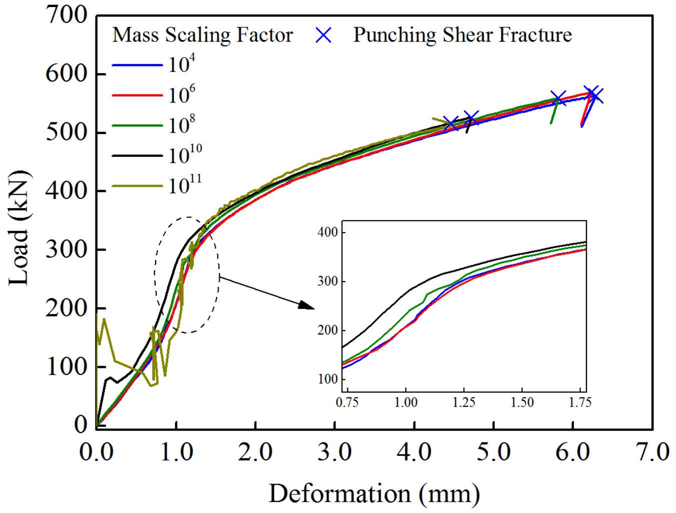

(b) Mass scaling factor

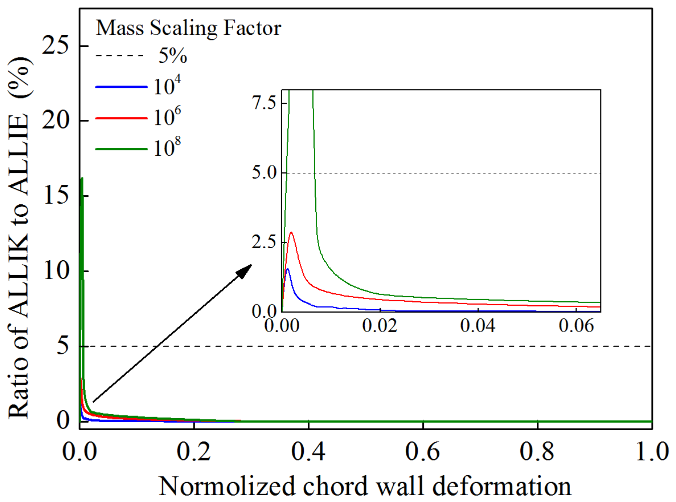

(c) Ratio of ALLIK to ALLIE

Fig. 7. Sensitive study of mesh and mass scaling factor

(T-240-3-500-12-AX)

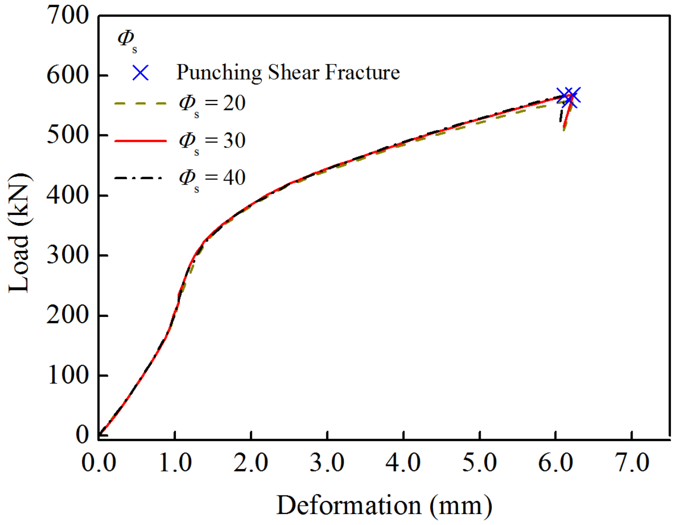

(a) Parameter of dilation angle (Φ_s)

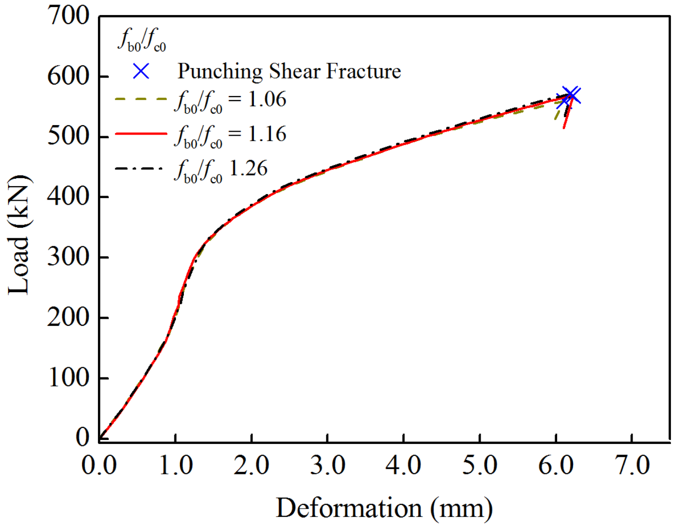

(b) Parameter of f_{bo}/f_{co}

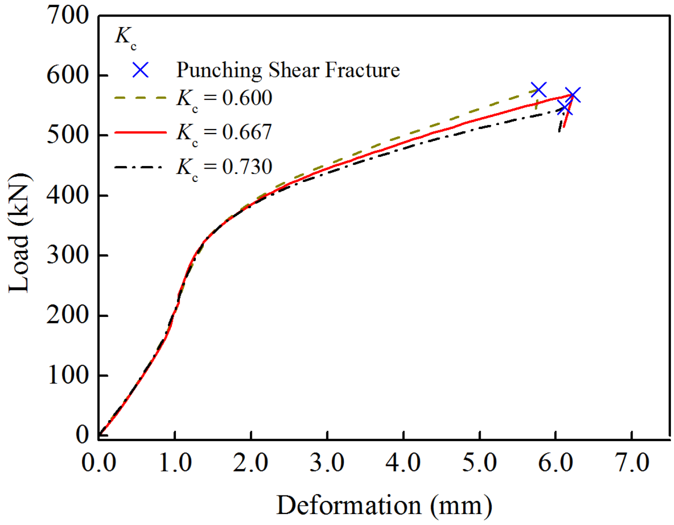

(c) Parameter of K_c

Fig. 8. Sensitive study on parameters of concrete damaged plasticity model in ABAQUS (T-240-3-500-12-AX)

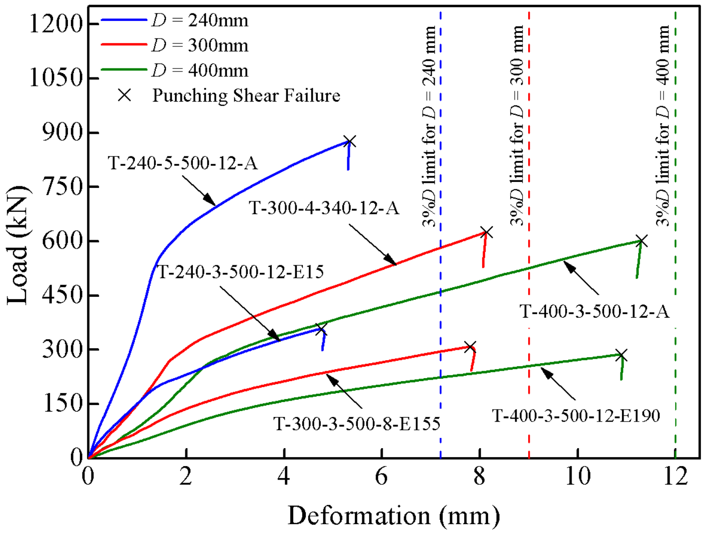

(a) Tension series

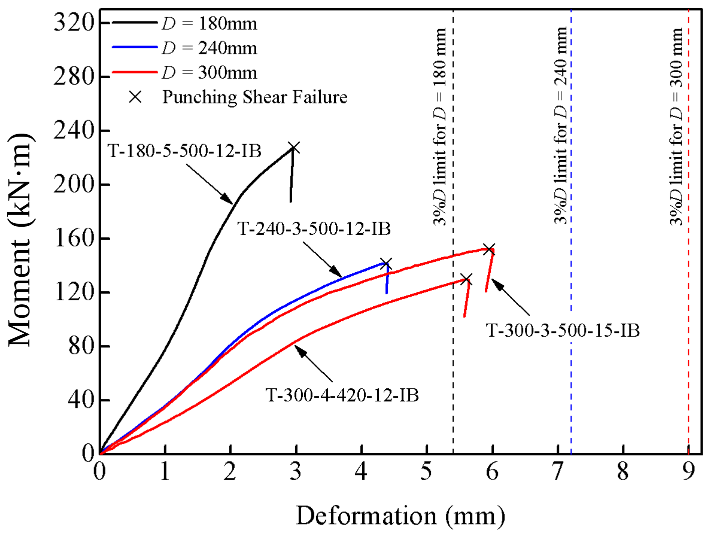

(b) In-plane bending series

Fig. 9. Load-deformation and moment-deformation curves from FEA results

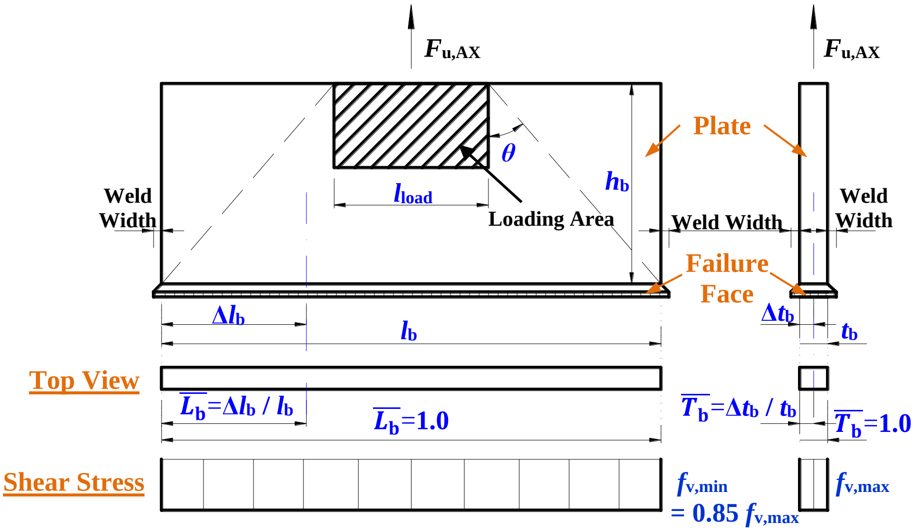

(a) Analytical model

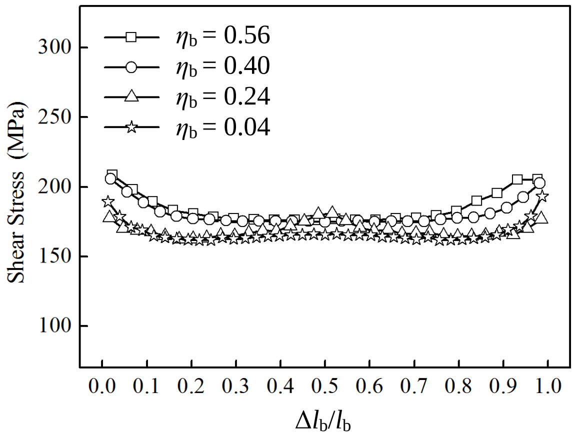

(b) Longitudinal stress distribution

Fig. 10. Analytical model and shear stress profile on the failure face for axial tensile connections

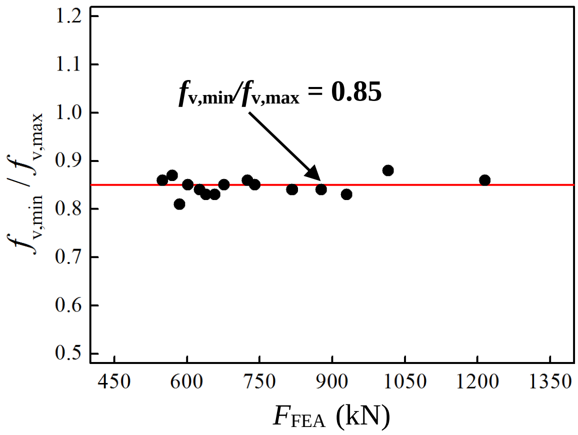

Fig. 11. Ratios of $f_{v,min}$ to $f_{v,max}$ for connections under axial tension

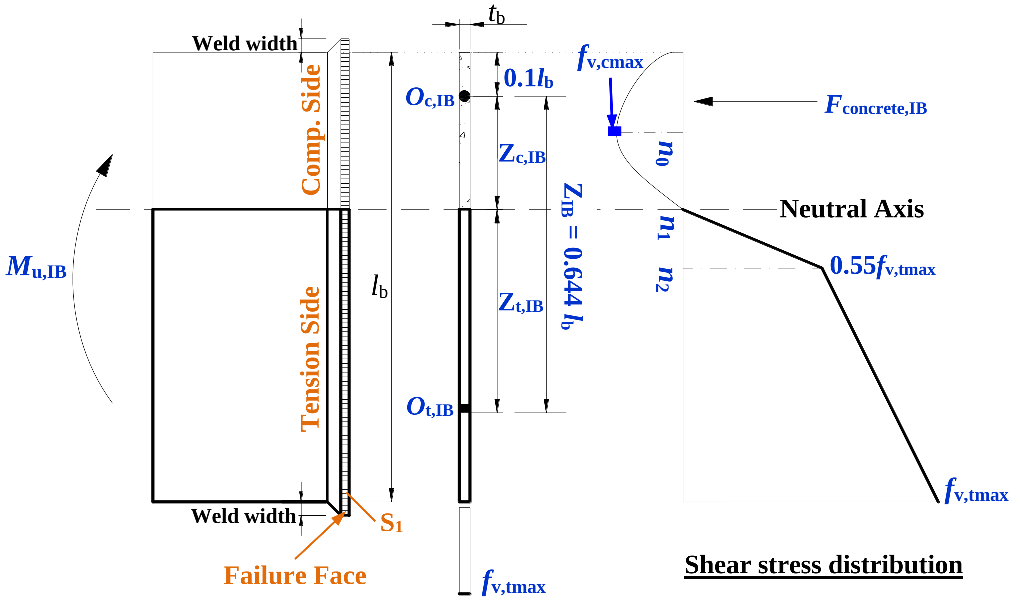

(a) Analytical model

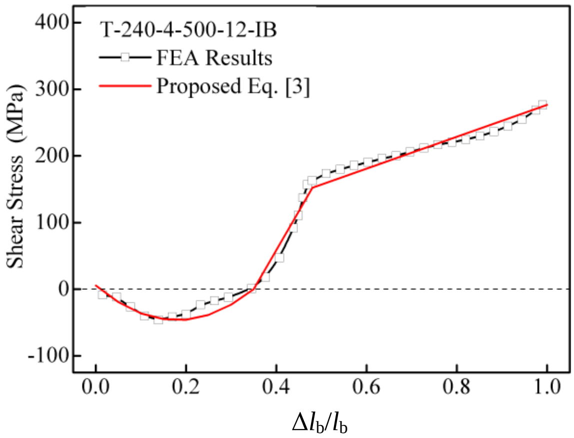

(b) T-240-4-500-12-IB

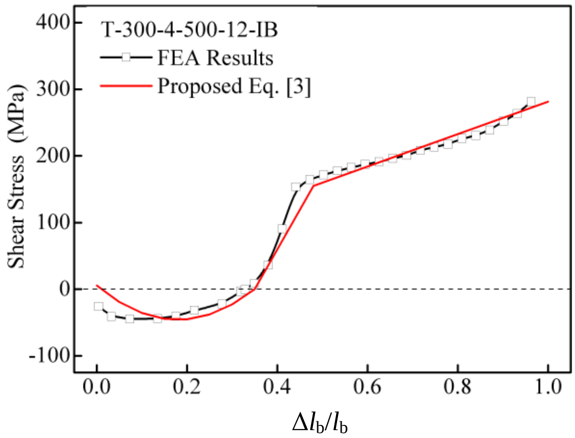

(c) T-300-4-500-12-IB

Fig. 12. Analytical model and shear stress profile on the failure face for in-plane bending connections

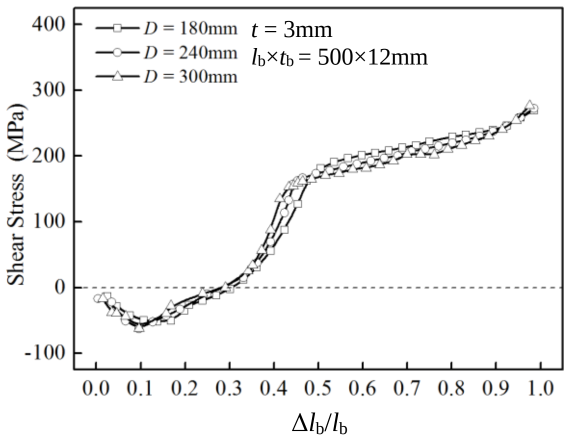

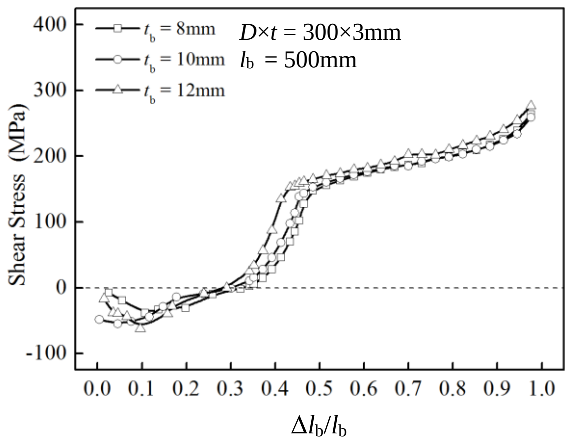

(a) Plate thickness t_b for in-plane bending (b) Chord diameter D for in-plane bending

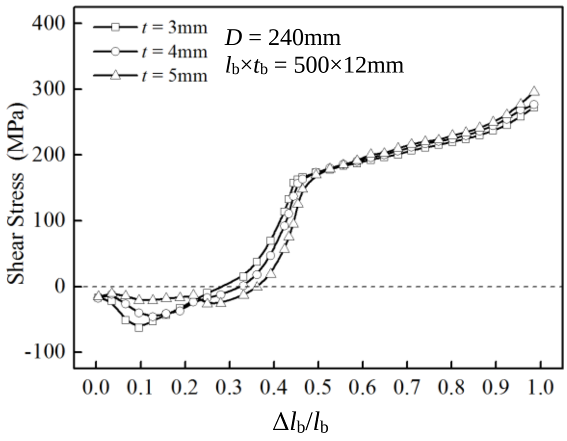

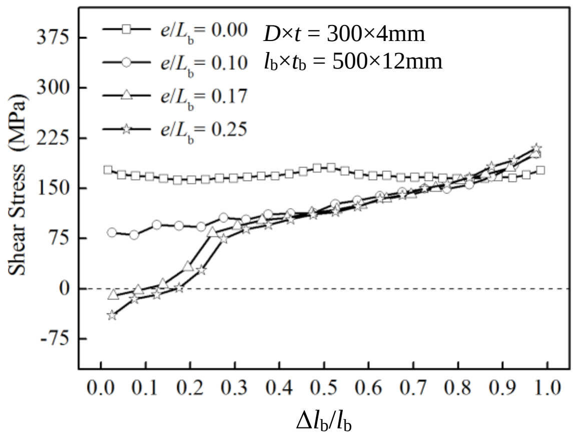

(c) Chord wall thickness t for in-plane bending (d) Eccentricity for tension

Fig. 13. Effects of parameters on the shear stress profiles on the failure face

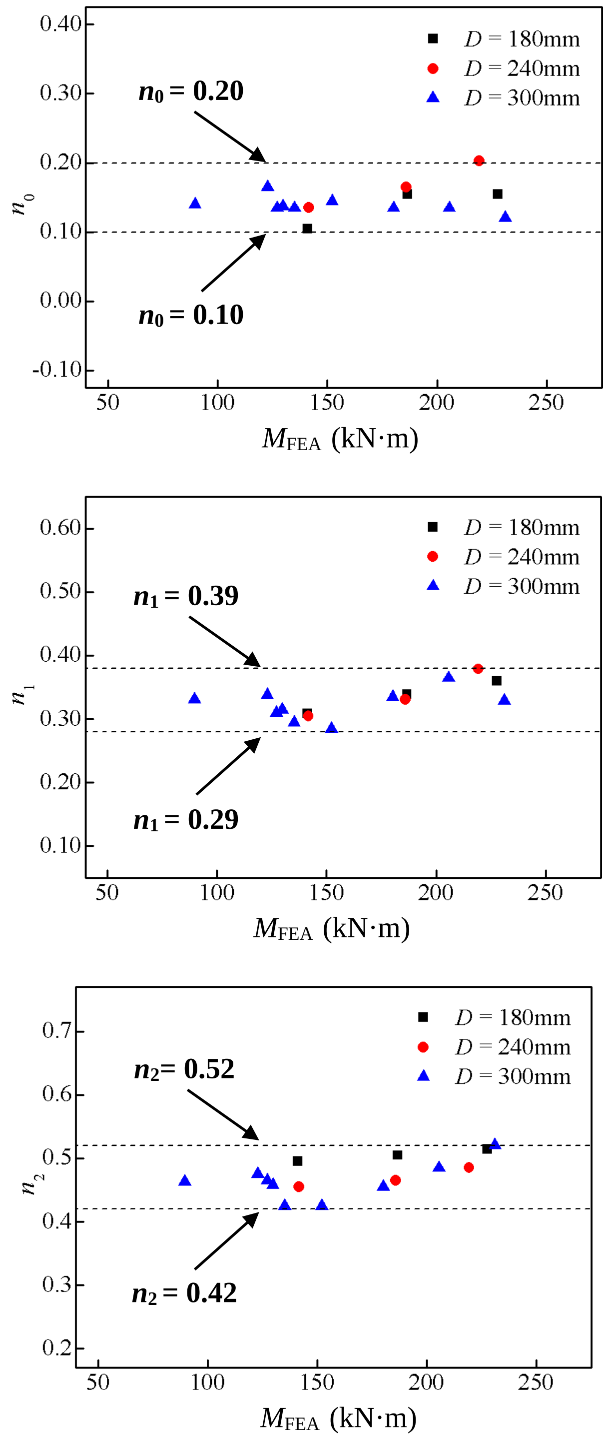

Fig. 14. Parametric study for connections under in-plane bending

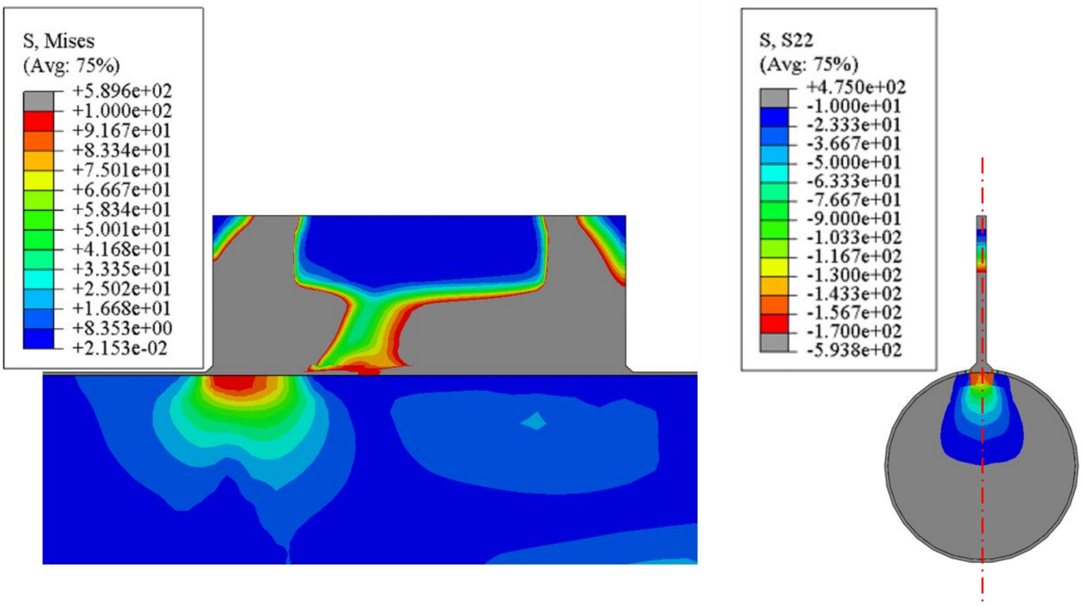

(a) Front view (b) Transvers view

Fig. 15. The von Mises stress and S22 distributions of the inside concrete on the compression side for T-240-4-500-12-IB

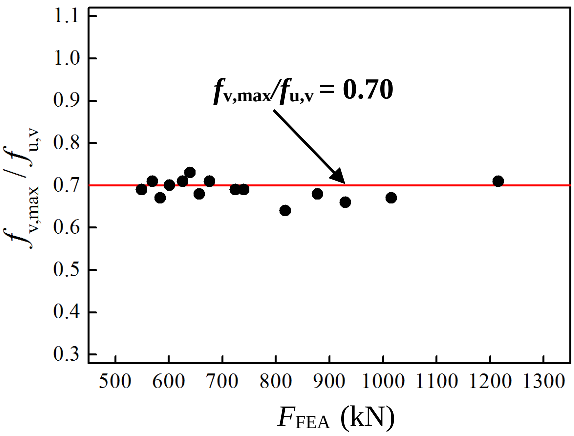

(a) Tension series

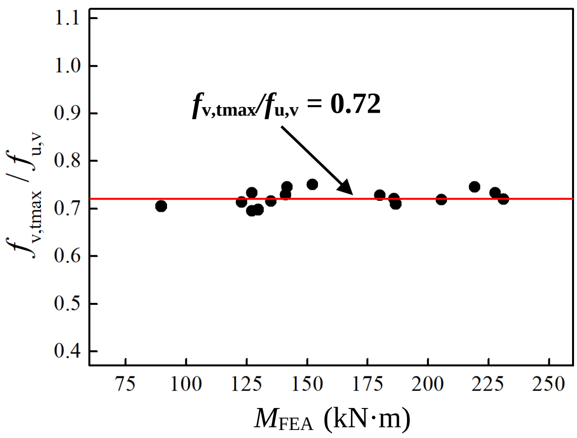

(b) In-plane bending series

Fig. 16. Ratios of the maximum stress on the failure face to steel ultimate strength

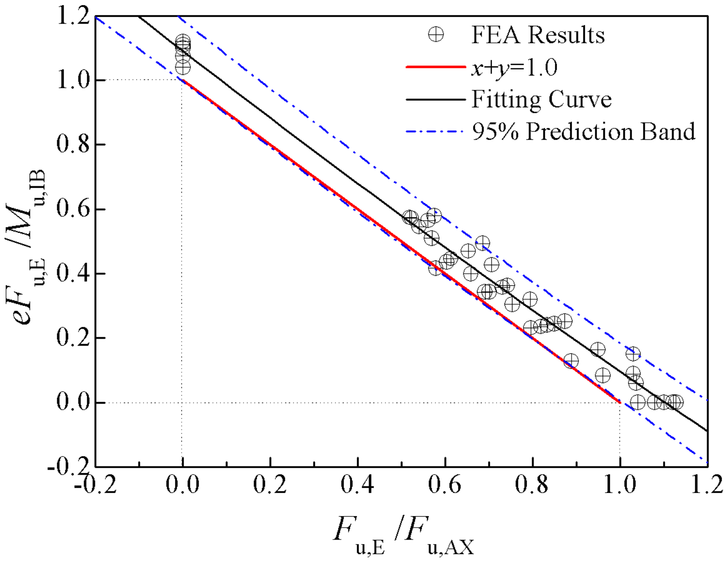

Fig. 17. Relationship between $F_{u,E}/F_{u,AX}$ and $eF_{u,E}/M_{u,IB}$

Table 1. Measured dimensions and ultimate strengths of test specimens

Specimens		Chord		Branch plate								
	L (mm)	D (mm)	t (mm)	l_b (mm)	t_b (mm)	h_b (mm)	F_{EXP} (kN)	M_{EXP} (kN·m)	F_{FEA}/ F_{EXP}	M_{FEA} / M_{EXP}	$F_{u,AX}$/ P_{EXP} or $F_{u,E}$/ P_{EXP}	$M_{u,IB}$/ M_{EXP}
T-300-4-AX	1394.7	300.9	3.95	498.3	11.86	191.6	843.7	—	0.99	—	0.85	—
T-300-4-AXR	1395.1	300.5	3.94	497.5	11.98	191.9	766.3	—	1.09	—	0.93	—
T-300-6-AX	1397.2	299.4	6.02	498.4	11.78	188.8	>980.0	—	N/A	—	N/A	—
T-300-4-E50	1397.8	299.8	3.94	497.8	11.89	189.0	652.1	—	0.97	—	0.85	—
T-300-4-E125	1395.1	300.1	4.05	498.2	11.79	190.1	464.4	—	1.04	—	0.89	—
T-300-4-IB	1994.9	300.6	3.98	498.8	11.88	191.5	—	165.27	—	1.09	—	1.02
T-300-5-IB	1995.7	300.4	4.91	498.3	11.92	191.2	—	203.82	—	1.03	—	0.99
T-300-5-IBR	1997.1	300.7	4.92	497.5	11.77	189.1	—	186.12	—	1.13	—	1.08
T-240-4-IB	1996.9	240.5	4.02	498.9	11.79	190.9	—	185.33	—	1.02	—	0.91
T-240-4-IBR	1996.0	240.9	3.91	499.0	11.89	189.1	—	195.76	—	0.97	—	0.86
T-240-5-IB	1994.7	240.3	4.95	498.2	11.92	191.2	—	212.40	—	1.02	—	0.95
CB0EA*	559.3	219.2	4.49	99.93	19.07	370.0	283.0	—	—	—	0.92	—
CB0FA*	558.9	219.2	4.49	100.3	18.99	370.0	328.0	—	—	—	0.80	—

Note: D: Outer diameter of the chord, t: Wall thickness of the chord, L: Length of the chord member, l_b: Length of the branch plate, t_b: Branch plate thickness, h_b: Branch plate height, AX: Axial loading, E: Eccentric loading, IB: In-plane bending, R: Repeat specimens.

*: Test data for longitudinal plate-to-CHS connection specimens failed at punching shear fracture of chord-wall from Ref. [6]. The ultimate tensile strength of steel for chord members is 527 MPa. It is noted that specimens CE0EA and CB0FA stand for unfilled and grouted connection respectively.

Table 2. Measured mechanical properties of the test specimens [10]

Steel		Nominal thickness (mm)	F_y (MPa)	F_u (MPa)	E (MPa)	ε_f (%)
Connections under axial, eccentric tension	Q235 (Chord)	4.0	269	385	2.04×10^5	32.6
	Q235 (Chord)	6.0	262	406	2.04×10^5	33.2
	Q345 (Brace)	6.0	330	485	1.99×10^5	34.0
	Q345 (Plate)	12.0	405	505	2.04×10^5	34.9
Connections under in-plane bending	Q345 (Chord)	4.0	439	522	2.06×10^5	29.7
	Q345 (Chord)	5.0	379	502	2.04×10^5	27.1
	Q345 (Brace)	6.0	388	509	2.00×10^5	32.0
	Q345 (Brace)	8.0	375	511	2.02×10^5	33.7
	Q345 (Plate)	12.0	443	524	2.04×10^5	32.9

Table 3. Parameters of MMC criterion used in FE models

Steel			F_y (MPa)	F_u (MPa)	Coefficients			
					c_1	c_2 (MPa)	A (MPa)	n
In validated FE models	Connections under axial, eccentric tension	4.0mm	269	385	0.12	288.8	660.0	0.207
		6.0mm	262	406	0.12	304.5	717.0	0.219
	Connections under in-plane bending	4.0mm	439	522	0.12	391.5	816.3	0.157
		5.0mm	379	502	0.12	376.5	844.9	0.181
In parametric study models			269	395	0.12	296.3	668.2	0.206
			439	520	0.12	390.0	815.0	0.155
			495	640	0.12	480.0	951.2	0.139

Table 4. Proposed design resistance of plate-to-concrete-filled CHS connections under tension and in-plane bending

Loading type		Punching shear design strength	Validity range
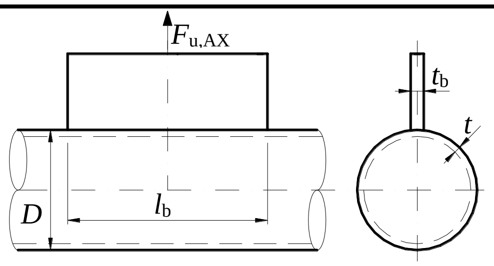	$\beta = t_b/D$ $\gamma = D/(2t)$ $\eta = l_b/D$	$F_{u,AX} = (0.9 l_b + 1.1 t_b)\ t\ F_u$ (6)	$0.02 \le \beta \le 0.06$ $20.0 \le \gamma \le 66.7$ $0.75 \le \eta \le 2.50$
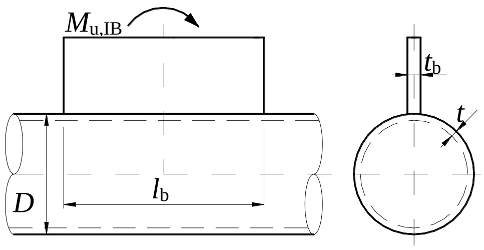	$\beta = t_b/D$ $\gamma = D/(2t)$ $\eta = l_b/D$	$M_{u,IB} = (0.31 l_b + 0.49 t_b) l_b\ t\ F_u$ (10)	$0.02 \le \beta \le 0.08$ $18.0 \le \gamma \le 66.7$ $0.85 \le \eta \le 3.33$
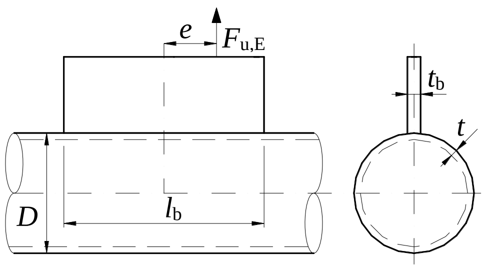	$\beta = t_b/D$ $\gamma = D/(2t)$ $\eta = l_b/D$	$\frac{F_{u,E}}{F_{u,AX}} + \frac{eF_{u,E}}{M_{u,IB}} \le 1.0$ (11)	$0.02 \le \beta \le 0.06$ $20.0 \le \gamma \le 66.7$ $0.85 \le \eta \le 2.50$

Table 5. Comparison of design strengths with FEA results: axial tension

Specimens	F_y (MPa)	F_u (MPa)	F_{FEA} (kN)	$F_{u,AX}$ (kN)	F_{u,AX_weld} (kN)	$F_{u,AX}/F_{FEA}$	$F_{u,AX\_weld}/F_{FEA}$
T-300-3-500-8-AX	269	395	584.2	543.7	576.9	0.93	0.99
T-300-3-500-10-AX	269	395	639.2	546.3	579.5	0.85	0.91
T-300-3-500-10-AX	439	520	843.6	719.2	762.8	0.85	0.90
T-300-3-500-10-AX	495	640	969.8	885.1	938.9	0.91	0.97
T-300-3-500-12-AX	269	395	656.6	548.9	582.1	0.84	0.89
T-300-3-500-15-AX	269	395	675.9	552.8	586.0	0.82	0.87
T-300-4-300-12-AX	269	395	549.2	447.5	491.7	0.81	0.90
T-300-4-340-12-AX	269	395	625.6	504.3	548.6	0.81	0.88
T-300-4-420-12-AX	269	395	740.1	618.1	662.3	0.84	0.89
T-300-4-500-12-AX	269	395	817.2	731.9	776.1	0.90	0.95
T-300-4-600-12-AX	269	395	929.7	874.1	918.3	0.94	0.99
T-300-5-500-12-AX	269	395	1015.4	914.8	970.1	0.90	0.96
T-300-6-500-12-AX	269	395	1215.2	1097.8	1164.1	0.90	0.96
T-240-3-500-12-AX	269	395	568.9	548.9	582.1	0.96	1.02
T-240-3-500-12-AX	439	520	738.7	722.6	766.3	0.98	1.04
T-240-3-500-12-AX	495	640	846.2	889.3	943.1	1.05	1.11
T-240-4-500-12-AX	269	395	724.5	731.9	776.1	1.01	1.07
T-240-5-500-12-AX	269	395	877.6	914.8	970.1	1.04	1.11
T-400-3-500-12-AX	269	395	601.5	548.9	582.1	0.91	0.97
					Mean	**0.91**	**0.97**
					CoV	**0.082**	**0.078**

Table 6. Comparison of design strengths with FEA results: in-plane bending

Specimens	F_y (MPa)	F_u (MPa)	M_{FEA} (kN·m)	$M_{u,IB}$ (kN·m)	M_{u_weld} (kN·m)	$M_{u,IB}$ / M_{FEA}	M_{u_weld} / M_{FEA}
T-300-3-500-8-IB	439	520	122.85	123.96	136.23	1.01	1.11
T-300-3-500-10-IB	269	395	98.45	94.74	104.07	0.96	1.06
T-300-3-500-10-IB	439	520	127.16	124.72	137.00	0.98	1.08
T-300-3-500-10-IB	495	640	160.74	153.50	168.62	0.95	1.05
T-300-3-500-12-IB	439	520	135.13	125.49	137.77	0.93	1.02
T-300-3-500-15-IB	439	520	152.12	126.63	138.93	0.83	0.91
T-300-4-340-12-IB	439	520	89.71	78.70	89.94	0.88	1.00
T-300-4-420-12-IB	439	520	129.79	118.88	132.70	0.92	1.02
T-300-4-500-12-IB	439	520	180.12	167.32	183.70	0.93	1.02
T-300-4-600-12-IB	439	520	231.11	239.47	259.06	1.04	1.12
T-300-5-500-12-IB	439	520	205.54	209.14	229.62	1.02	1.12
T-240-3-500-12-IB	439	520	141.66	125.49	137.77	0.89	0.97
T-240-4-500-12-IB	439	520	185.92	167.32	183.70	0.90	0.99
T-240-5-500-12-IB	269	395	170.95	158.87	174.43	0.93	1.02
T-240-5-500-12-IB	439	520	219.26	209.14	229.62	0.95	1.05
T-240-5-500-12-IB	495	640	274.70	257.41	282.61	0.94	1.03
T-180-3-500-12-IB	439	520	141.13	125.49	137.77	0.89	0.98
T-180-4-500-12-IB	269	395	143.39	127.10	139.54	0.89	0.97
T-180-4-500-12-IB	439	520	186.63	167.32	183.70	0.90	0.98
T-180-4-500-12-IB	495	640	230.43	205.93	226.09	0.89	0.98
T-180-5-500-12-IB	439	520	227.72	209.14	229.62	0.92	1.01
T-400-3-500-12-IB	439	520	127.12	125.49	137.77	0.99	1.08
					Mean	**0.93**	**1.03**
					CoV	**0.055**	**0.052**

Table 7. Comparison of design strengths with FEA results: eccentric tension

Specimens	F_y (MPa)	F_u (MPa)	F_{FEA} (kN)	$F_{u,E}$ (kN)	F_{u,E_Weld} (kN)	$F_{u,E}$ / F_{FEA}	F_{u,E_Weld} / F_{FEA}
T-300-4-500-12-E15	269	395	750.75	673.7	716.4	0.90	0.95
T-300-4-500-12-E30	269	395	691.87	624.1	665.3	0.90	0.96
T-300-4-500-12-E50	269	395	619.18	568.2	607.4	0.92	0.98
T-300-4-500-12-E70	269	395	578.77	521.6	558.8	0.90	0.97
T-300-4-500-12-E85	269	395	540.83	491.4	527.2	0.91	0.97
T-300-4-500-12-E105	269	395	514.59	456.1	490.2	0.89	0.95
T-300-4-500-12-E125	269	395	499.91	425.5	458.1	0.85	0.92
T-300-4-500-12-E175	269	395	420.75	364.5	393.6	0.87	0.94
T-300-3-500-8-E25	269	395	481.07	475.1	506.4	0.99	1.05
T-300-3-500-8-E50	269	395	450.93	421.9	451.2	0.94	1.00
T-300-3-500-8-E70	269	395	408.05	387.2	415.1	0.95	1.02
T-300-3-500-8-E85	269	395	351.00	364.7	391.6	1.04	1.12
T-300-3-500-8-E105	269	395	356.72	338.5	364.1	0.95	1.02
T-300-3-500-8-E125	269	395	326.71	315.8	340.2	0.97	1.04
T-300-3-500-8-E155	269	395	308.33	286.9	309.7	0.93	1.00
T-300-3-500-8-E175	269	395	292.26	270.4	292.2	0.93	1.00
T-300-3-500-12-E25	269	395	563.18	479.8	511.1	0.85	0.91
T-300-3-500-12-E50	269	395	435.13	426.2	455.6	0.98	1.05
T-300-3-500-12-E85	269	395	377.75	368.5	395.4	0.98	1.05
T-300-3-500-12-E125	269	395	334.81	319.2	343.6	0.95	1.03
T-300-3-500-12-E190	269	395	283.34	262.1	283.2	0.93	1.00
T-400-3-500-12-E10	269	395	566.93	519.0	551.4	0.92	0.97
T-400-3-500-12-E50	269	395	477.49	426.2	455.6	0.89	0.95
T-400-3-500-12-E85	269	395	383.22	368.5	395.4	0.96	1.03
T-400-3-500-12-E125	269	395	316.37	319.2	343.6	1.01	1.09
T-400-3-500-12-E190	269	395	285.89	262.1	283.2	0.92	0.99
T-240-3-500-12-E15	269	395	525.22	505.3	537.3	0.96	1.02
T-240-3-500-12-E50	269	395	447.66	426.2	455.6	0.95	1.02
T-240-3-500-12-E85	269	395	399.61	368.5	395.4	0.92	0.99
T-240-3-500-12-E125	269	395	356.96	319.2	343.6	0.89	0.96
T-240-3-500-12-E175	269	395	314.31	273.4	295.2	0.87	0.94
					Mean	**0.93**	**1.00**
					CoV	**0.048**	**0.048**